

## **Hysteresis loss in NdFeB Permanent Magnets in a Permanent-Magnet-Synchronous Machine**

Egorov Dmitry, Petrov Ilya, Pyrhönen Juha, Link Joosep, Stern Raivo, Sergeant Peter, Sarlioglu Bulent

This is a Final draft version of a publication  
published by IEEE  
in IEEE Transactions on Industrial Electronics

**DOI:** 10.1109/TIE.2021.3050358

### **Copyright of the original publication:**

© Copyright 2021 IEEE

### **Please cite the publication as follows:**

Egorov, D., Petrov, I., Pyrhönen, J., Link, J., Stern, R., Sergeant, P., Sarlioglu, B. (2021).  
Hysteresis loss in NdFeB Permanent Magnets in a Permanent-Magnet-Synchronous Machine.  
IEEE Transactions on Industrial Electronics. DOI: 10.1109/TIE.2021.3050358

**This is a parallel published version of an original publication.  
This version can differ from the original published article.**

# Hysteresis loss in NdFeB Permanent Magnets in a Permanent-Magnet-Synchronous Machine

Dmitry Egorov, Ilya Petrov, Juha Pyrhönen, *Senior Member, IEEE*, Joosep Link, Raivo Stern, *Member, IEEE*, Peter Sergeant, *Senior Member, IEEE*, and Bulent Sarlioglu, *Senior Member, IEEE*

**Abstract**—Most permanent-magnet (PM) loss studies consider only eddy current loss and neglect hysteresis. In this paper, the hysteresis behavior of two NdFeB PM grades with different magnetic properties is assessed when applied in a PMSM. Data from vibrating sample magnetometer measurements and hysteresis modelling are used as a base. In addition to the main magnetic phase the samples contained magnetic phases with reduced coercivity. Such phases may contribute to hysteresis losses in a PM material. A new model is introduced to simulate the hysteresis of rare-earth magnets of any geometric shape in the 2<sup>nd</sup> and 1<sup>st</sup> quadrants of the intrinsic  $BH$ -plane. The magnetic field strength distribution in the permanent magnet material of an electrical motor was analyzed by 2D finite-element method (FEM). The results are used as the input data for an analytical hysteresis model. The results indicate that the hysteresis loss resulting from the structural imperfections and geometry of the magnet may introduce a considerable loss in NdFeB PMs applied in rotating electrical machines.

**Index Terms**—Electric machines, neodymium magnets, loss measurement, magnetic field measurement, magnetic hysteresis, magnetic losses, magnetic materials, permanent magnets, permanent magnet machines.

## I. INTRODUCTION

PERMANENT MAGNET (PM) rotating electrical machines are developed intensively to meet the energy-efficiency improvement requirements. The Rare-Earth (RE) PMs (e.g., SmCo and NdFeB) enable PM electrical machine designs with superior efficiency and power or torque density [1].

The design of a high-efficiency PM electrical machine requires detailed analysis of possible loss components. In addition, the PM material itself is prone to losses that are difficult to evaluate precisely. Usually only eddy-current losses are evaluated in magnets during the typical design routine of PM-based electrical machine. This approach is based on thinking that in ideal permanent magnets no hysteresis losses can take place. This is, however, not the case with real permanent magnets and hysteresis losses can take place in them. Analytical and Finite Element (FE) methods estimating the PM eddy current loss are frequently discussed in the literature [2].

Several studies, however, report that, in addition to eddy current loss, the possibility for hysteresis loss must be analyzed in a real PM material, if it is used in a rotating electrical machine [3]-[8]. The alternating current (AC) magnetic field losses in Nd-based magnets are measured in [3] and [4] with nearly similar devices. Initially fully polarized PM samples are placed in a gapless magnetic circuit and the measured losses are separated to eddy current loss and hysteresis loss by the two-frequency method. The results indicate that in some normal-operation modes considerable amounts of hysteresis loss can be present. The measured data of PM loss only under AC fields in [3] are further used in the post-processing of the FE calculated magnetic flux density distribution in PMs of a rotor-surface-magnet PM Synchronous Machine (PMSM). The calculated PM hysteresis loss is more than double the value of the eddy current loss. The calculation procedure in [3] ignores the effect of the demagnetizing field to the hysteresis loss in actual machine. In practice, the working point of a PM (applied in a machine) in the  $BH$ -plane has an extra self-demagnetization field resulting from the air gap and non-infinite permeability of the electric steel, which shift operating point deeper in the 2<sup>nd</sup> quadrant of the  $BH$ -plane [9]. Measurement results with similar measurement device in [4] clearly indicate that the hysteresis loss in PM is significantly mitigated if negative direct current (DC) field is acting at the PM sample. Thus, the loss estimation procedure in [3] is not suitable for investigation of the hysteresis loss in electrical machines having the air gap as a natural demagnetization factor. It overestimates the PM hysteresis loss.

A general discussion on the PM hysteresis loss in sintered NdFeB magnets is provided in [5]. The measured data in [5] are limited by several recoil loops. The loops clearly depict that the formation of considerable hysteresis loops is possible in Nd-based PMs in the normal operation of some RE PM machines.

A high-accuracy measurement system based on the Vibrating Sample Magnetometer (VSM) is used to study the hysteresis behavior of three PM grades (NdFeB, SmCo, and Ferrite) in [6]. The calculated hysteresis loss in NdFeB PMs of the rotor-surface-magnet PMSM with external rotor topology is up to 1.4% of the studied machine's output power. The limited measured

data, the measurement temperature of 23 °C, and the inappropriate treatment of the VSM output make the results in [6] questionable from the rotating electrical machinery point of view, i.e. the methodology in [6] may overestimate the actual hysteresis loss in PM motors.

Detailed investigations of the hysteresis loss in ferrite PMs are reported in [7], [8] via VSM measurements for four distinct grades, in total. The hysteresis behavior of ferrite magnets is simulated with a static History Dependent Hysteresis Model (HDHM) and the total hysteresis loss is calculated in the PMs of two different PMSM designs. The results in [7], [8] show that significant hysteresis loss is possible also in ferrite PMs under operation conditions that regularly move back and forth between the 2<sup>nd</sup> and the 1<sup>st</sup> quadrant of the  $BH$ -plane. The relatively small coercivity of ferrite PMs restricts the maximum possible armature reaction in the machine to avoid irreversible demagnetization. Therefore, only a small volume of ferrite magnets may be subject to considerable hysteresis loss. The studies [7], [8] are limited to ferrite magnets.

Based on our best knowledge, there are no accurate studies of the hysteresis loss phenomenon in NdFeB magnets of PM electrical machines. The geometrical and magnetic properties of RE magnets make this type of PM vulnerable to hysteresis loss in the rotating electrical machinery [8].

The paper is organized as follows. Section II describes the possible origin of the hysteresis loss in Nd-based PMs, the measurement procedure, and the analytical modelling principle. The hysteresis loss is estimated analytically using FE estimated field-strength behavior in a PMSM with outer rotor topology and rotor surface magnets in Section III. Section IV discusses the results. Section V concludes the paper.

## II. METHODS

### A. Origin of the hysteresis loss in NdFeB PMs

Hysteresis theory is the basic theory for the magnetic materials [10]. The relative permeability of practical NdFeB magnets  $\mu_r \approx 1.01$ – $1.05$  [10] differs from the relative permeability of vacuum. This is an indication of a fact that there are some magnetically soft phases in the material also enabling hysteresis in a PM sample. Numerous studies report that, in addition to the Nd<sub>2</sub>Fe<sub>14</sub>B main hard magnetic phase, an NdFeB magnet may contain magnetic regions with clearly lower coercivities [4], [10]–[17]. These regions may be located either on the surface or inside of the PM volume.

PM's surface defects are studied and discussed in [4], [10]–[12]. The analysis in [4], [10] refers to the oxidation as the origin for reduced-coercivity magnetic phases on PM. The surface oxidation of an NdFeB magnet results in the formation of hexagonal Nd<sub>2</sub>O<sub>3</sub> and  $\alpha$ -Fe magnetic phases with coercivities in the range of 50–200 kA/m (at ambient temperature) and a depth of around 10 nm at the surface of Nd-Fe-B grains [10]. The demagnetization of a NdFeB magnet is governed by the nucleation mechanism, which promotes the reversal of the surface layer of a PM (typical thickness 10–20  $\mu$ m) [4], [10]. The study [4] estimates that the coercivity of the magnetic phases on the surface of the Nd PMs is only around 11%–35% of the coercivity of the main hard magnetic phase at the temperature range of

22–180 °C. The Kerr microscopy images (by Evico Magnetics GmbH) in [4] support the assumption about the reduced coercivity of the magnetic phases on the surface, i.e. surface-located grains of initially fully polarized PM sample experience significant irreversible demagnetization under demagnetizing magnetic field strengths notably smaller than the intrinsic coercivity of the main hard magnetic phase.

Studies [11], [12] refer to the machining stresses on the damaged layer on the surface of NdFeB PMs. The cutting and grinding process of a bulk magnet removes part of Nd-rich phase volumes from the surface-located grains and as a result the magnetic interaction between the grains on the surface increases. The nucleation coercivity mechanism of NdFeB PM promotes the polarity reversal in the surface layer within the depth of the mean grain diameter. The measured main  $BH$ -curves demonstrate the presence of the magnetic phases with coercivities 13%–33% of the coercivity of the main hard magnetic phase in [11], and 31% in [12]. Studies [11], [12] demonstrate that sample heat treatment with temperature exceeding the melting point of the Nd-rich phase and the formation of a magnetic-insulating layer on the surface reduces the share of the magnetic phases with degraded coercivity. Nevertheless, a sample ideally consisting of just one main hard magnetic phase has never been demonstrated in practice. There are always some defects in a real PM material resulting in a relative permeability higher than unity which demonstrates the non-perfect nature of practical PM materials.

Reduced coercivity magnetic phases may be also located in the bulk volume of a magnet. The presence of  $\alpha$ -Fe, FeB, and Nd<sub>2</sub>O<sub>3</sub> magnetic phases have been reported inside NdFeB magnets [13]–[16]. The Nd-rich phase has the strongest effect on the coercivity of the PM, and it is usually non-homogeneous with respect to thickness and chemical composition [13], [14]. Therefore, a general analysis of the volumetric defects in sintered NdFeB magnet is difficult. Studies [15], [17] investigate the magnetic behavior of sintered NdFeB magnets with sophisticated analysis of the measured First Order Reversal Curves (FORCs). The studies provide evidence that the magnetic phases with coercivities around 40% to 80% of expected PM coercivity may originate from either Nd- $f$  site (see e.g. Fig. 4 in [15]) or Nd-rich phase, and, therefore, these phases may be an intrinsic property of a sintered NdFeB magnet. The estimated coercivities of these phases are in the range of 374–636 kA/m (at room temperature), and, therefore, they unlikely originate from the oxidation or machining of the PM surface [15].

Based on the results discussed above, this study assumes the following: 1) magnetic phases with coercivities around 11%–35% of the coercivity of the main magnetic phase are located on the surface of the sample. These phases originate either from the surface layer oxidation or from the machining process; 2) magnetic phases with coercivities 40%–80% of the main magnetic phase coercivity are located in the bulk volume of a PM sample. These phases may be associated with the Nd-rich layer or Nd- $f$  site, and they are an internal property of an Nd PM.

### B. Measurement setup and data treatment

The test installation comprises a Physical-Properties-Measurement System with up to 14 Tesla superconducting magnets, P525 VSM, and a data acquisition system by Quantum Design. The intrinsic properties of PM, i.e. polarization  $J$  with respect

to the intrinsic field strength  $H_i$ , are obtained from VSM-measured data according to the procedure introduced in [18].

The VSM measures the sum of the responses of all magnetic phases accumulated within one measurement signal of the sample. Reduced-coercivity magnetic phases may have a distinct contribution and the magnetic properties of the magnets can have certain discrepancy even in the samples from the same batch. Thus, several samples of the same grade must be measured and analyzed to get a more accurate picture of the distribution of the magnetic phases in a PM grade. The studied NdFeB PMs are uncoated samples of 512a and 793a grades supplied by Neorem Oy. The dimensions of the samples are  $3 \times 3 \times 2(M\uparrow\uparrow)$ ,  $3 \times 3 \times 3.8(M\uparrow\uparrow)$ ,  $2 \times 2 \times 1.7(M\uparrow\uparrow)$ ,  $2 \times 2 \times 3(M\uparrow\uparrow)$ ,  $3 \times 3 \times 0.5(M\uparrow\uparrow)$ ,  $3 \times 3 \times 1(M\uparrow\uparrow)$ ,  $2 \times 2 \times 0.7(M\uparrow\uparrow)$  mm<sup>3</sup> for 512a grade and  $3 \times 3 \times 2(M\uparrow\uparrow)$ ,  $3 \times 3 \times 0.5(M\uparrow\uparrow)$ ,  $3 \times 3 \times 1(M\uparrow\uparrow)$ ,  $2 \times 2 \times 0.7(M\uparrow\uparrow)$  mm<sup>3</sup> for 793a grade, respectively. The measurement temperature is set to 80 °C, which may be a representative PM operating temperature in an electrical machine [9]. The measurement sequence included the measurement of the main demagnetization curves. The distribution of the magnetic phases is analyzed with the following optimization function which was derived from the original idea published in [19]:

$$\begin{cases} J(H) = \sum_{i=1}^3 \left[ V_i \cdot \left( J_i \cdot \tanh(\lambda_i \cdot (H + H_{c,j,i})) + \mu_0 \cdot \xi \cdot H + C_i \right) \right], \\ \sum_{i=1}^3 V_i = 1 \end{cases} \quad (1)$$

where  $V_i, J_i, \lambda_i, H_{c,j,i}$  are the relative volume, remanent polarization, steepness coefficient, and intrinsic coercivity of the  $i^{\text{th}}$ -magnetic phase of the sample,  $C_i = 0$  is the parameter needed for the analysis. The parameter  $\xi$  is small in practice, and it is referred as a measurement error e.g. in [20]. The measured and fitted with (1) main demagnetization curves are depicted in Fig. 1. The distributions of the magnetic phases estimated with (1) for the samples studied are depicted in Fig. 2.

The data in Fig. 2 demonstrate the same trend for each measured sample. The main magnetic phase 1 with the highest coercivity  $H_{c,j,1}$  has the dominant volumetric share  $V_1$ , whereas the shares  $V_2$  and  $V_3$  of the magnetic phases with reduced coercivities  $H_{c,j,2}$  and  $H_{c,j,3}$  are markedly lower. The magnetic phases with reduced coercivities have  $H_{c,j,2} = (0.23\text{--}0.31)H_{c,j,1}$ ,  $H_{c,j,3} = (0.38\text{--}0.61)H_{c,j,1}$  for 512a grade, and  $H_{c,j,2} = (0.16\text{--}0.31)H_{c,j,1}$ ,  $H_{c,j,3} = (0.55\text{--}0.68)H_{c,j,1}$  for 793a grade, respectively.

The distributions obtained for  $H_{c,j,2}$  and  $H_{c,j,3}$  are well in the ranges of the results in [4], [10]–[17], as it was discussed earlier. The median values for the relative volumes of volume-located magnetic phases with the reduced coercivities  $V_3 = 0.029$  and  $V_3 = 0.075$  are estimated from data in Fig. 2 for the grades 512a and 793a, respectively. The height of the damaged layer on the surface of the  $i^{\text{th}}$ -sample  $h_{\text{layer},i}$  may be calculated from the geometric dimensions of the sample and the data in Fig. 2 as:

$$h_{\text{layer},i} = V_{2,i} \cdot (S/V)^{-1}. \quad (2)$$

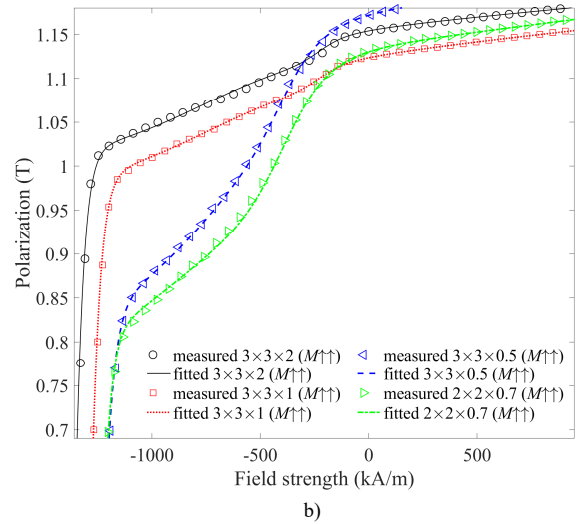
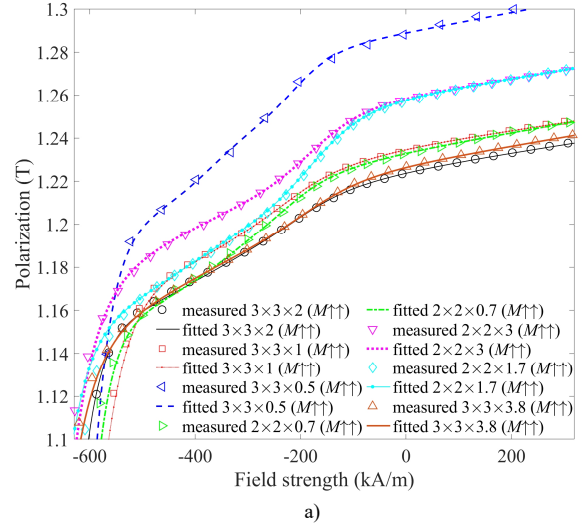


Fig. 1. Main demagnetization curves of NdFeB PMs measured and fitted with (2) a) grade 512a, b) grade 793a.

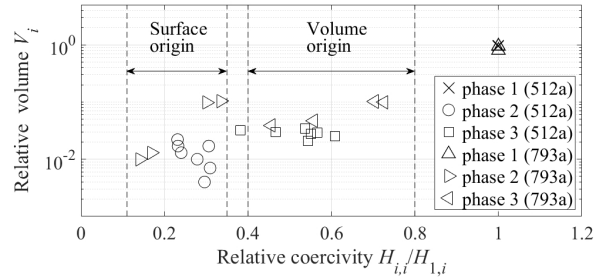


Fig. 2. The distributions of the magnetic phases estimated with (1) in the samples studied. The coercivities of the magnetic phases for each sample measured are represented with respect to the coercivity  $H_{c,j,1}$  of the main magnetic phase 1 with the dominant volumetric share  $V_1$ .

The calculated median values are  $h_{\text{layer}} = 9.48 \mu\text{m}$  and  $h_{\text{layer}} = 6.68 \mu\text{m}$  for 512a and 793a grades, respectively. The grain size of the commercial NdFeB magnets is reported in the range of 5–15  $\mu\text{m}$  [4], [11], [13], [21]–[23]. Therefore, the statistically estimated median heights of the damaged surface layer are

physically feasible, and they are used as reference values in the modelling of the hysteresis loss phenomenon in the PM magnetic poles described further.

### C. Modelling of the hysteresis loss in PMs

The measured main demagnetization curves of the samples in Fig. 1 are formed by several magnetic phases with different properties. In addition, the surface-located layer of the magnetic phases with reduced coercivity causes the main demagnetization curve to depend on the size of a magnet. There are several modelling concepts to simulate the PM hysteresis. Detailed reviews may be found in [7], [8], [24]. Most hysteresis models are developed for the materials consisting of one magnetic phase, and, thus, require modification for the case studied.

The modelling concept in this study develops further the simulation principle introduced in [7], [8]. The hysteresis behavior of an NdFeB PM is represented by artificial ‘hard’ and ‘soft’ magnetic phases acting simultaneously. The ‘soft’ magnetic phase is actually hard in its nature [25], but it is called ‘soft’ just because of the presence of the magnetic phase with clearly higher coercivity. The ‘hard’ magnetic phase represents the hysteresis behavior of the volume-located magnetic phases, i.e. phase 1 and phase 3. The ‘soft’ magnetic phase (i.e. phase 2) represents the contribution of the surface-located magnetic phases with reduced coercivity. The hysteresis behavior of each artificial magnetic phase is simulated by the static version of HDHM [26]. The HDHM may be substituted with other hysteresis modelling alternatives that obey the most relevant Madelung rules for magnetic hysteresis [7], [8].

The HDHM concept enables the simulation of a part of a material’s  $JH$ -curve, which considerably reduces the measurement data needed. The procedure for building the model and parameter identification is presented for 512a grade as an example:

#### 1) Step 1. Creation of the main loops for the ‘hard’ and ‘soft’ magnetic phases

The measurement data is acquired from the  $3 \times 3 \times 2(M\uparrow\uparrow)$  mm<sup>3</sup> PM sample in 2<sup>nd</sup> and 1<sup>st</sup> quadrants of the intrinsic  $BH$ -plane at 80 °C. The simulation region is constrained within  $(H_{lim,1}, H_{lim,2})$  by the part of the main demagnetization curve  $desc(H)$  and first Order Reversal Curve (ORC)  $acs(H)$ , as it is depicted in Fig. 3. The basic principle of HDHM is shown in Fig. 4. The magnetic properties of the phases are estimated with (1), where the relative volumes of the magnetic phases with reduced coercivity  $V_2$  and  $V_3$  are no more optimization variables. The values of  $V_3$  are equal to the median values estimated in the previous subsection. The value of  $V_2$  is estimated from the sample geometry with (2) and the calculated median values  $h_{layer}$  for each PM grade, respectively. The descending main branch of each magnetic phase must follow the return-point-memory rule, i.e.:

$$\begin{cases} J_{acs,i}(H_{lim,1}) = J_{des,i}(H_{lim,1}), \\ J_{acs,j}(H_{lim,2}) = J_{des,j}(H_{lim,2}) \end{cases} \quad (3)$$

The condition (3) makes  $H_{c,j,i}$  and  $\lambda_i$  to be the only optimization variables in (1) when ascending main curves are estimated, whereas the other parameters are calculated as:

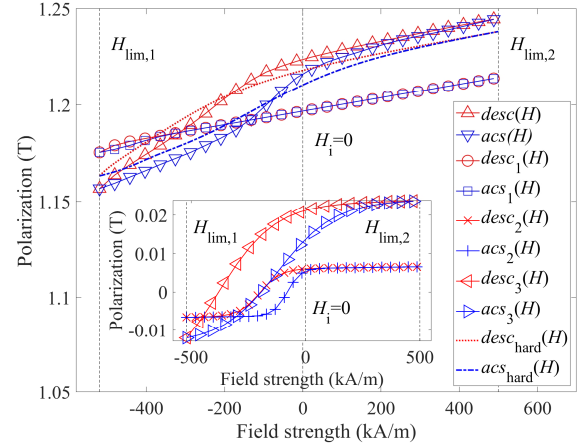


Fig. 3. Identification of the major loops for ‘soft’ and ‘hard’ magnetic phases (512a grade). The artificial ‘hard’ magnetic phase is formed by the magnetic phases 1 and 3 acting simultaneously. The ‘soft’ magnetic phase is represented by the magnetic phase 2 and it relates to the surface located magnetic layer.

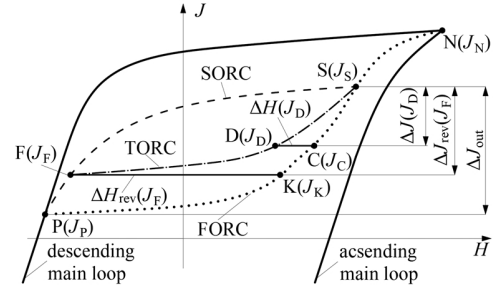


Fig. 4. The HDHM principle. The ascending  $H_{acs}(J)$  and descending  $H_{des}(J)$  branches of the outer loop for the third ORC (TORC) F-D-S ( $n = 3$ , dash-dotted line) are formed with the second ORC (SORC) S-F-P ( $n = 1$ , dashed line) and the first ORC (FORC) P-K-S-N ( $n = 2$ , dotted line), respectively. These are known from the previous magnetization history. The magnetic field strength at arbitrary point  $D$  with polarization value  $J_D$  belonging to the constructed TORC F-D-S is calculated from respective point  $C$  ( $J_D = J_C$ ) belonging to  $H_{acs}(J)$  with a correction by  $\Delta H(J_D)$  (9). The hysteresis behavior of the recoil curves obeys the return point memory effect, i.e. the  $n^{\text{th}}$  reversal curve ends at the starting point of the  $(n - 1)^{\text{th}}$  reversal curve (TORC F-D-S ends at point  $S$  from which SORC S-F-P originates). Following the wiping out property rule, the value of the magnetic field strength exceeding that in point  $S$  propagates the operating point of a magnet along the  $(n - 2)^{\text{th}}$  reversal curve (S-N part of FORC P-K-S-N as if the recoil loop S-F-D-S had never existed).

$$C_i = \frac{Z_1 \cdot y_i(H_{lim,2}) - Z_2 \cdot y_i(H_{lim,1}) + V_i \cdot (M_1 Z_2 - M_2 Z_1)}{V_i \cdot (Z_1 - Z_2)}, \quad (4)$$

$$J_i = \frac{y_i(H_{lim,1}) - V_i \cdot M_1}{V_i \cdot Z_1} - \frac{Z_1 \cdot y_i(H_{lim,2}) - Z_2 \cdot y_i(H_{lim,1}) + V_i \cdot M_1 \cdot Z_2 - V_i \cdot M_2 \cdot Z_1}{V_i \cdot Z_1 \cdot (Z_1 - Z_2)}, \quad (5)$$

$$y_i(H) = V_i \cdot \left( J_i \cdot \tan(\lambda_i \cdot (H + H_{c,j,i})) + \mu_0 \cdot \xi \cdot H \right), \quad (6)$$

$$Z_1 = \tanh(\lambda_i \cdot (H_{lim,1} + H_{c,j,i})), \quad (7)$$

$$Z_2 = \tanh(\lambda_i \cdot (H_{lim,2} + H_{c,j,i}))$$

$$\begin{aligned} M_1 &= \mu_0 \cdot \xi \cdot H_{\text{lim},1} \\ M_2 &= \mu_0 \cdot \xi \cdot H_{\text{lim},2} \end{aligned} \quad (8)$$

The data estimated with (1), (4)–(8) are depicted in Tables I–II for 512a and 793a grades, respectively.

2) *Step 2. Parameter identification procedure of HDHM for artificial ‘hard’ and ‘soft’ magnetic phases*

The details of HDHM may be found e.g. in [7], [26] with concise discussions and application examples, therefore, the modelling concept is discussed only briefly in this paper. The  $n^{\text{th}}$  order reversal curve is estimated from the  $(n-1)^{\text{th}}$  and  $(n-2)^{\text{th}}$  reversal curves, which form the current outer loop and are always known from the previous magnetization history. The current reversal curve is constructed with the gap  $\Delta H(J)$  [8]:

$$\begin{aligned} \Delta H(J) &= \\ \Delta H_{\text{rev}}(J_{\text{RC}}) &\cdot \left[ 1 - ((b-d) \cdot \frac{\Delta J(J)}{\Delta J_{\text{rev}}} + d) \right] \cdot e^{-a \cdot \Delta J_{\text{rev}} \left( 1 - \frac{\Delta J(J)}{\Delta J_{\text{rev}}} \right)}, \quad (9) \\ &+ (H_{\text{asc}}(J) - H_{\text{des}}(J)) \cdot \left( (b-d) \cdot \frac{\Delta J(J)}{\Delta J_{\text{rev}}} + d \right) \end{aligned}$$

where  $J_{\text{RC}}$  is the polarization value at the reversal point,  $H_{\text{asc}}(J)$  and  $H_{\text{des}}(J)$  describe the ascending and descending branches of the current outer loop, and  $\Delta H_{\text{rev}}(J_{\text{RC}}) = H_{\text{asc}}(J_{\text{RC}}) - H_{\text{des}}(J_{\text{RC}})$ . Fig. 4 demonstrates the calculation principle for  $\Delta H(J)$  and  $\Delta J_{\text{rev}}$  for the third ORCs as an example. The behavior of the constructed reversal curve depends on its starting point at the current outer loop. It is described by a set of coefficients  $\alpha(\beta) > 0$ ,  $0 \geq d(\beta) \geq 1$  that are estimated based on the measured hysteresis behavior of the PM. The parameter  $\beta$  depends on  $\Delta J_{\text{rev}}$  and the height of the current outer loop  $\Delta J_{\text{out}}$ :

$$\beta = \frac{\Delta J_{\text{rev}}}{\Delta J_{\text{out}}} \quad (10)$$

Parameter identification procedure was conducted for the ascending and descending curves separately based on the first order reversal curves and several recoil loops, which are measured in the region of interest. Fig. 5 depicts the coefficients esti-

Branch	Calculated parameters
descend- ing	$J_1 = 1.261 \text{ T}$ , $\lambda_1 = 0.017$ , $H_{c,j,1} = 715.129 \text{ kA/m}$ , $J_2 = 0.2811 \text{ T}$ , $\lambda_2 = 0.011$ , $H_{c,j,2} = 199.236 \text{ kA/m}$ , $J_3 = 0.8055 \text{ T}$ , $\lambda_3 = 0.004$ , $H_{c,j,3} = 384.127 \text{ kA/m}$
ascending	$J_1 = 0.0017 \text{ T}$ , $\lambda_1 = 0.0186$ , $H_{c,j,1} = 418.941 \text{ kA/m}$ , $J_2 = 0.2809 \text{ T}$ , $\lambda_2 = 0.0170$ , $H_{c,j,2} = 80.4567 \text{ kA/m}$ , $J_3 = 0.6294 \text{ T}$ , $\lambda_3 = 0.0041$ , $H_{c,j,3} = 122.9603 \text{ kA/m}$ , $C_1 = 1.2593$ , $C_2 = 2 \times 10^{-4}$ , $C_3 = 0.1827$
Common parameters	$\zeta = 0.02948$ , $V_2 = 0.0219$ , $V_3 = 0.029$ , $H_{\text{lim},1} = -519.7 \text{ kA/m}$ , $H_{\text{lim},2} = 500 \text{ kA/m}$

Branch	Calculated parameters
descend- ing	$J_1 = 1.213 \text{ T}$ , $\lambda_1 = 0.009$ , $H_{c,j,1} = 1499.9 \text{ kA/m}$ , $J_2 = 0.701 \text{ T}$ , $\lambda_2 = 0.011$ , $H_{c,j,2} = 211.057 \text{ kA/m}$ , $J_3 = 0.595 \text{ T}$ , $\lambda_3 = 0.002$ , $H_{c,j,3} = 683.837 \text{ kA/m}$
ascending	$J_1 = 0.0009 \text{ T}$ , $\lambda_1 = 0.0233$ , $H_{c,j,1} = 950.445 \text{ kA/m}$ , $J_2 = 0.701 \text{ T}$ , $\lambda_2 = 0.0125$ , $H_{c,j,2} = 48.896 \text{ kA/m}$ , $J_3 = 0.5319 \text{ T}$ , $\lambda_3 = 0.0017$ , $H_{c,j,3} = 249.769 \text{ kA/m}$ , $C_1 = 1.212$ , $C_2 = 2.25 \times 10^{-9}$ , $C_3 = 0.0697$
Common parameters	$\zeta = 0.01818$ , $V_2 = 0.015$ , $V_3 = 0.075$ , $H_{\text{lim},1} = -1100 \text{ kA/m}$ , $H_{\text{lim},2} = 1220 \text{ kA/m}$

ated for the model. Figs. (6)–(7) demonstrate a comparison of the measured and model-simulated results for 512a grade and 793a grade, respectively. The model-estimated hysteresis behavior of magnets is used to evaluate the amount of the hysteresis loss in PMs of an electrical machine.

### III. RESULTS

A power-dense tooth-coil-winding rotor-surface-magnet PMSM with an outer rotor was studied in terms of hysteresis losses. The design topology chosen is reported to have a high magnetic field strength variation in the PMs because of the rotor-surface PMs, tooth-coil-windings, and the relatively wide slot openings [8], Table III. The PMSM topology is depicted in Fig. 8 for the motor design with 793a grade as an example. Each PM is sliced with  $w_1 = 1$  plane parallel to  $lh$ -plane and  $w_2 = 32$  planes parallel to  $hw$ -plane, i.e. segmented into 66 equal pieces with dimensions  $20 \times 3 \times 9(M\uparrow\uparrow) \text{ mm}^3$  to reduce eddy current loss in the magnets.

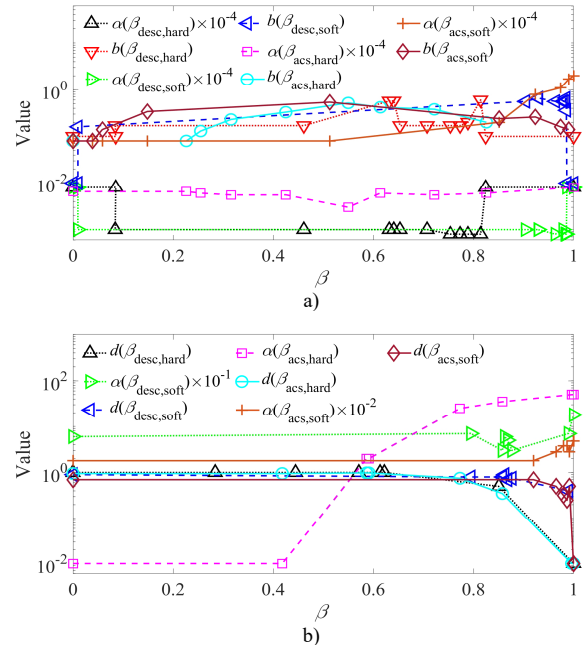


Fig. 5. Coefficients determined for HDHM during parameter identification procedure for the ascending and descending reversal curves of artificial ‘hard’ and ‘soft’ magnetic phases for NdFeB PM. a) 512a grade,  $d_{\text{acs},i}(\beta) = b_{\text{acs},i}(\beta)$ ,  $d_{\text{des},i}(\beta) = b_{\text{des},i}(\beta)$ ; b) 793a grade,  $b_{\text{acs},i}(\beta) = 0$ ,  $b_{\text{des},i}(\beta) = 0$ ,  $a_{\text{hard},\text{des}}(\beta) = 10^{-5}$ .



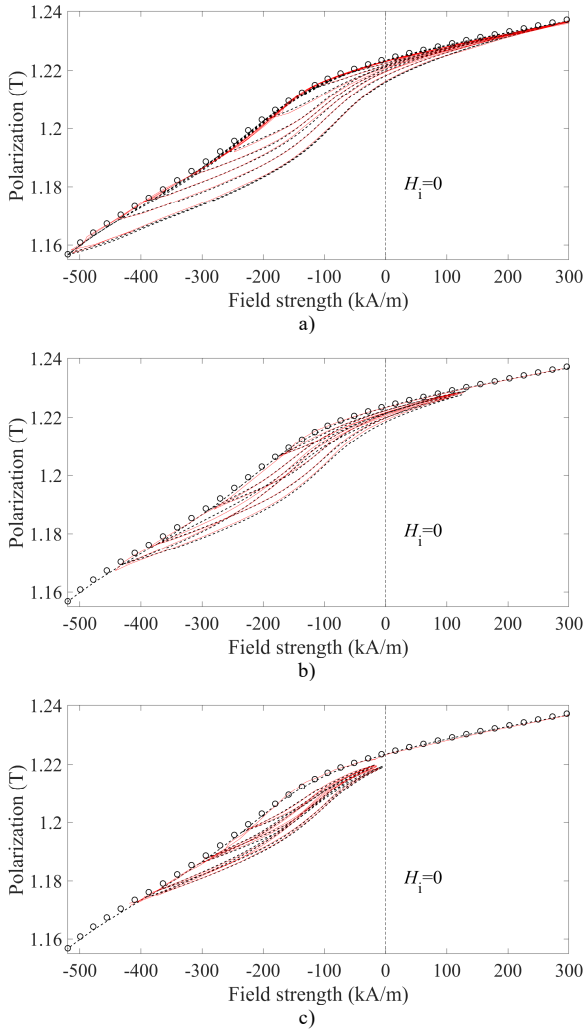


Fig. 6. Comparison of the measured (solid red line) and model-simulated (dashed line) hysteresis behavior for  $3 \times 3 \times 2(M\uparrow\uparrow)$  PM sample of grade 512a at  $80^\circ\text{C}$ . The main  $JH$ -curve is depicted with circle markers. a) set of FORCs; b) hysteresis behavior of PM when the external field is strong enough to move the operating point of PM from the 2<sup>nd</sup> to the 1<sup>st</sup> quadrant of the intrinsic  $JH$ -plane and backwards, respectively; c) hysteresis behavior of PM in the 2<sup>nd</sup> quadrant of the intrinsic  $JH$ -plane.

The PM hysteresis loss calculation procedure develops further the principles introduced in [8]. The PM poles of the machine are divided into  $k_1 = 11$  layers along PM's height with  $k_2 = 201$  points in each layer, that is,  $11 \times 201 = 2211$  elemental volumes. The magnetic field strength variation in each PM volume is calculated with 2D FLUX<sup>TM</sup> by Altair for time  $t_v$ :

$$t_v = \frac{1}{f} \cdot \frac{2p}{Q_s}, \quad (11)$$

where  $p$  is the number of pole pairs,  $f$  is the electrical frequency, and  $Q_s$  is the number of the stator slots. The time period  $t_v$  determines the smallest time when every elemental volume of the machine's magnetic pole is exposed to all possible values of the magnetic field strength during a specific operation mode. The FE-calculated magnetic field strength values are used as the input data for the introduced modelling approach. The hysteresis

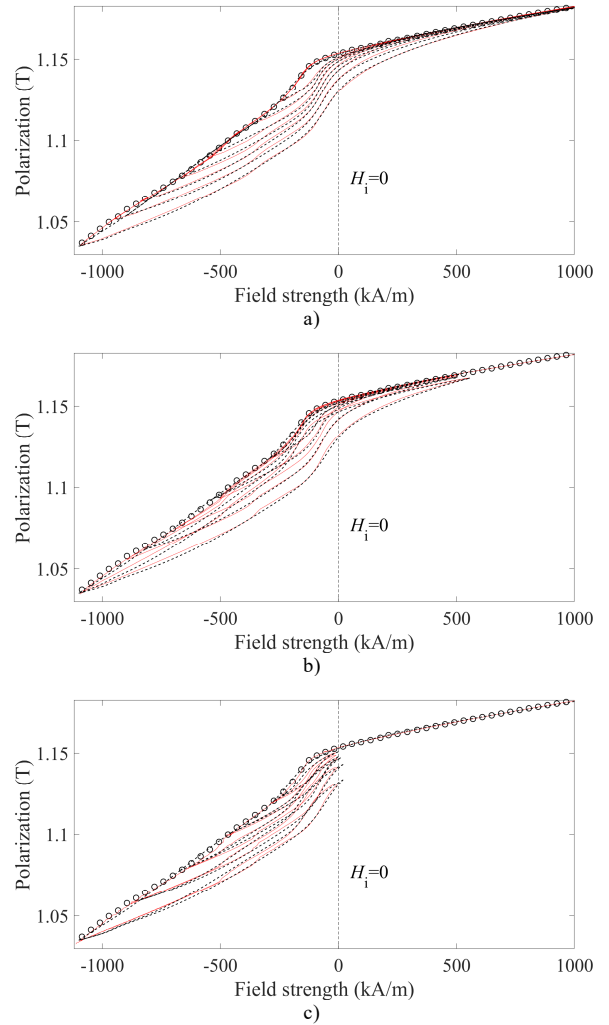


Fig. 7. Comparison of the measured (solid red line) and model-simulated (dashed line) hysteresis behavior for  $3 \times 3 \times 2(M\uparrow\uparrow)$  PM sample of grade 793a at  $80^\circ\text{C}$ . The main  $JH$ -curve is depicted with circle markers. a) set of FORCs; b) hysteresis behavior of PM when the external field is strong enough to move the operating point of PM from the 2<sup>nd</sup> to the 1<sup>st</sup> quadrant of the intrinsic  $JH$ -plane and backwards, respectively; c) hysteresis behavior of PM in the 2<sup>nd</sup> quadrant of the intrinsic  $JH$ -plane.

loss in the PMs of the machine designs studied are calculated as the sum of the losses in the PM volume created by the 'hard' magnetic phases  $E_{\text{hyst,hard}}$  and the losses at the surface of PM created by the 'soft' magnetic phases  $E_{\text{hyst,soft}}$ :

$$E_{\text{hyst,hard}} = \frac{2 \cdot p \cdot V_{\text{hard}}}{(1 - V_2) \cdot k_1 \cdot k_2 \cdot t_v} \left( \sum_{i=1}^{k_1} \sum_{j=1}^{k_2} E_{\text{hard},i,j} \right), \quad (12)$$

$$V_{\text{hard}} = h_{\text{PM}} l_{\text{PM}} w_{\text{PM}} - (h_{\text{PM}} l_{\text{PM}} + l_{\text{PM}} w_{\text{PM}} + h_{\text{PM}} w_{\text{PM}} + h_{\text{PM}} w_1 l_{\text{PM}} + w_2 h_{\text{PM}} w_{\text{PM}}) \cdot 2 \cdot h_{\text{layer}}, \quad (13)$$

TABLE III  
PARAMETERS AND DIMENSIONS OF THE OBSERVED PMSMs

Parameter	Value
Air-gap length $\delta$ [m]	$1.2 \times 10^{-3}$
Electrical frequency $f$ [Hz]	1666.6
Machine length in the axial direction $l$ [m]	0.099
Number of pole pairs $p$	10
Number of series turns per phase per stator $N$	40
Number of stator slots $Q_s$	24
Period when magnetic field values at each magnet point are repeated $t_v$ [s]	$5 \times 10^{-4}$
Permanent magnet height $h_{PM}$ [m]	0.009
Permanent magnet width $w_{PM}$ [m]	0.04
Permanent magnet length in axial direction $l_{PM}$ [m]	0.099
Rated speed $n_{rated}$ [rpm]	10000
Ratio of slot opening to tooth tip width $b_{si}$	0.46
Rotor external radius $r_{re}$ [m]	$158 \times 10^{-3}$
Rotor internal radius $r_{si}$ [m]	$135 \times 10^{-3}$
Stator external radius $r_{se}$ [m]	$133.8 \times 10^{-3}$

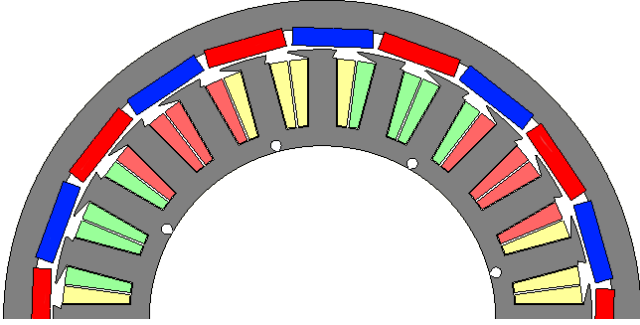


Fig. 8. The PMSM design topology with 793a PM grade.

$$E_{\text{hyst,soft}} = \frac{2 \cdot p \cdot h_{\text{layer}}}{t_v \cdot V_2} \cdot \left( \frac{h_{PM} l_{PM}}{k_1} \sum_{i=1}^{k_1} \sum_{j=1, k_2} E_{\text{soft},i,j} + \frac{w_{PM} l_{PM}}{k_2} \sum_{i=1, k_1} \sum_{j=1} E_{\text{soft},i,j} + \frac{2 \cdot w_{PM} h_{PM}}{k_1 k_2} \sum_{i=1}^{k_1} \sum_{j=1} E_{\text{soft},i,j} + \frac{2 \cdot h_{PM} \cdot l_{PM}}{k_1} \sum_{i=1}^{k_1} \sum_{j=1}^{w_1} E_{\text{soft},i, \left( \frac{k_2 \cdot j}{1+w_1} \right)} + \frac{2 \cdot w_2 \cdot w_{PM} h_{PM}}{k_1 k_2} \sum_{i=1}^{k_1} \sum_{j=1}^{k_2} E_{\text{soft},i,j} \right) \quad (14)$$

Fig. 9 depicts the calculated loss distribution in the PM region and FE-calculated maximum/minimum values of magnetic field strength for an electrical machine design with 793a PM grade at the nominal load as an example. The calculated eddy current loss and hysteresis loss in the PM material with respect to the load are presented in Fig. 10.

#### IV. DISCUSSION

The spatial distribution of the volumetric hysteresis loss in Fig. 9(a) is typical for the chosen design topology [7], [8]. Fig. 9(c) shows the highest magnetic field strength variation on the surface of the PM close to the airgap region as the combined effect of armature reaction spatial harmonics of current fundamental, slotting effect, and tooth tip leakage flux [9]. The dis-

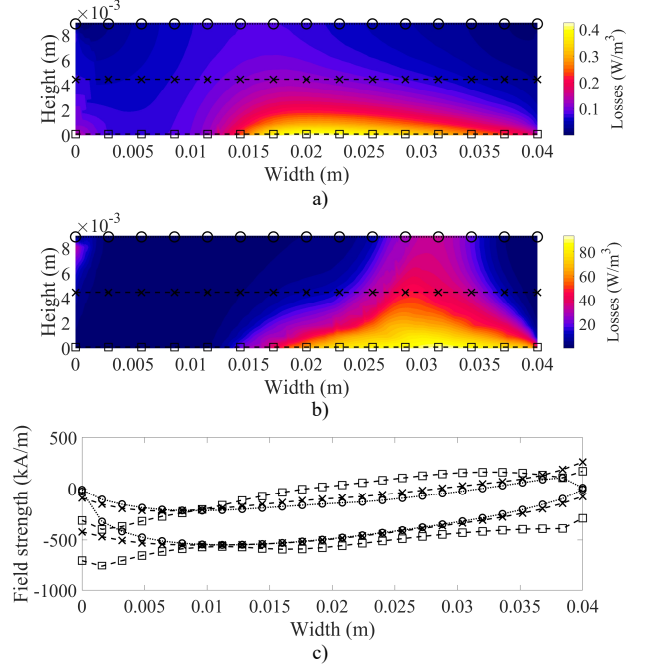


Fig. 9. Model-calculated hysteresis loss distribution and FE-simulated maximum/minimum field strength in the PM region at nominal load (793a grade). a) Hysteresis loss in the PM's volume generated by the 'hard' magnetic phase; b) Hysteresis loss at the PM's surface along the machine's radial direction generated by the 'soft' magnetic phase (per single layer at the surface of PM); c) Maximum and minimum values of the magnetic field strength in the PM domain at the surface (close to the air gap, square-dashed line), middle (cross-dashed line), and bottom (close to the rotor hub, circle-dotted line). The rotor rotates counterclockwise.

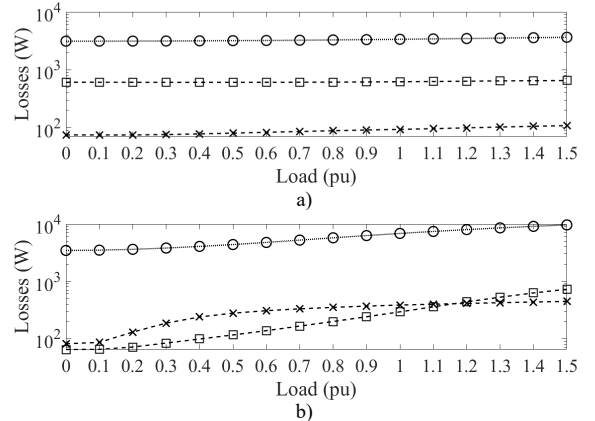


Fig. 10. Eddy current loss (circle-dotted line), hysteresis loss generated by the 'soft' magnetic phase (cross-dashed line), and hysteresis loss generated by the 'hard' magnetic phase (square-dashed line) in PMs as a function of machine's load. a) PMSM design with 512a grade; b) PMSM design with 793a grade. The nominal output power and nominal phase current of the studied PMSM topology are 524 kW and 247 A<sub>RMS</sub>, and 1556 kW and 1060 A<sub>RMS</sub> for electrical machine design with 512a grade and 793a grade, respectively.

ussed phenomena are mitigated deeper in the magnet. Therefore, the largest share of the hysteresis loss generated by the 'hard' magnetic phase is located close to the airgap. The minimum/maximum values of the magnetic field strength in the middle of the PM region and close to the rotor hub are not strong enough to cause the formation of the recoil loops with considerable amount of energy in phase 1 and phase 3.



The spatial location of the surface-located hysteresis loss along the machine's radial direction is depicted in Fig. 9(b). It follows the same trend as in Fig. 9(a), which is dictated by the time and spatial distribution of the magnetic field strength in PM domain during the machine's operation. However, the narrow region in Fig. 9(b) along the machine's radial direction generates a comparable value of hysteresis loss as in the regions close to the airgap. The data in Table II and in Fig. 9(c) show that the magnetic field strength variation in some PM parts deeper in the magnet is in the suitable range to cause significant demagnetization and magnetization of phase 2.

The model-simulated data in Fig. 9(a)-(b) show that the hysteresis loss generated by the 'soft' magnetic phase on the surface of the PM is several orders of magnitude higher than the hysteresis loss in the volume of the PM in the 'hard' magnetic phases. This corresponds to the results available in the literature [3], [4], [10], [11], [22]. Nevertheless, the shares of the surface- and volume-located hysteresis loss in Fig. 10 are different in the studied PMSMs, although they have similar geometrical dimensions.

The slotting effect and the tooth tip leakage flux have a higher effect on the total magnetic field variation inside the PMs compared with the armature reaction effect in the design with 512a grade as the relatively low coercivity of this grade restricts the armature current to around 25% in comparison to the PM motor with 793a PM grade. Fig. 3, Fig. 6(c), and the data in Table I show the volume-located magnetic phase 3 has a higher polarization value in comparison to the surface-located regions formed by the phase 2.

The 'hard' magnetic phase can form hysteresis loops with considerable amount of energy already in the 2<sup>nd</sup> quadrant of the intrinsic *JH*-plane. In PMSM with 512a magnets the volume-located hysteresis loss is dominant, Fig. 10(a). In Fig. 10(b) the PM-surface hysteresis loss is larger than the volume-located hysteresis loss up to  $1.2 \times$  the nominal load in the PMSM design with the 793a grade. The armature reaction field is strong enough to cause the formation of considerable recoil loops by the 'soft' magnetic phase (Figs. 7 and 9). The hysteresis loss created by the 'soft' magnetic phase increases relatively fast in the load range 0.1 – 0.4 pu. A notable amount of the regions on the surface of the PM are prone to partial demagnetization at relatively low values of armature current. The hysteresis loss in the volume of the PM increase with the load of the machine and exceeds the surface-located hysteresis loss at around 1.2 pu load. The data in Fig. 10 demonstrate that the hysteresis losses are around 20% and 10% of the eddy current losses in 512a grade and 793a grade magnets respectively.

## V. CONCLUSION

Structural imperfections in real RE PMs can generate a significant hysteresis loss under the operating conditions in an electrical machine. The PM hysteresis loss may originate either from the volume- or surface-located magnetic phases with reduced coercivity. The PM segmentation is an effective means to reduce the eddy current loss in PMs. However, it creates a layer of damaged grains on PM surfaces, which may increase the hysteresis loss in the material. This study is limited to a single machine topology having a very high specific power and is

therefore more vulnerable to armature reaction caused problems in the PMs than average PM motors.

## REFERENCES

- [1] V. Madonna, P. Giangrande, L. Lusuadi, A. Cavallini, C. Gerada and M. Galea, "Thermal overload and insulation aging of short duty cycle, aerospace motors," *IEEE Trans. Ind. Electron.*, vol. 67, DOI 10.1109/TIE.2019.2914630, no. 4, pp. 2618-2629, Apr. 2020.
- [2] D. Ouamara and F. Dubas, "Permanent-magnet eddy-current losses: a global revision of calculation and analysis," *Math. Comput. Appl.*, vol. 24, no. 3, pp. 1-18, Jul. 2019.
- [3] A. Fukuma, S. Kanazawa, D. Miyagi and N. Takahashi, "Investigation of AC loss of permanent magnet of SPM motor considering hysteresis and eddy-current losses," *IEEE Trans. Magn.*, vol. 41, DOI 10.1109/TMAG.2005.846282, no. 5, pp. 1964-1967, May 2005.
- [4] M. Moore, S. Roth, A. Gebert, L. Schultz and O. Gutfleisch, "The effect of surface grain reversal on the AC losses of sintered Nd-Fe-B permanent magnets," *J. Magn. Magn. Mat.*, vol. 375, DOI 10.1016/j.jmmm.2014.09.047, pp. 43-48, Sep. 2015.
- [5] J. Pyrhönen, S. Ruoho, J. Nerg, M. Paju, S. Tuominen, H. Kankaanpää, R. Stern, A. Boglietti and N. Uzhegov, "Hysteresis losses in sintered NdFeB permanent magnets in rotating electrical machines," *IEEE Trans. Ind. Electron.*, vol. 62, DOI 10.1109/TIE.2014.2354597, no. 2, pp. 857 - 865, Jan. 2015.
- [6] I. Petrov, D. Egorov, J. Link, R. Stern, S. Ruoho and J. Pyrhonen, "Hysteresis losses in different types of permanent magnets used in PMSMs," *IEEE Trans. Ind. Electron.*, vol. 64, DOI 10.1109/TIE.2016.2548440, no. 3, pp. 2502-2510, Mar. 2016
- [7] D. Egorov, I. Petrov, J. Link, R. Stern and J. J. Pyrhönen, "Model-based hysteresis loss assessment in PMSMs with ferrite magnets," *IEEE Trans. Ind. Electron.*, vol. 65, DOI: 10.1109/TIE.2017.2714121, no. 1, pp. 179-188, Jan. 2018.
- [8] D. Egorov, I. Petrov, J. Pyrhönen, J. Link and R. Stern, "Hysteresis loss in ferrite permanent magnets in rotating electrical machinery," *IEEE Trans. Ind. Electron.*, vol. 65, no. 12, pp. 9280-9290, Dec. 2018.
- [9] J. Pyrhönen, T. Jokinen and V. Hrabovcova, *Design of Rotating Electrical Machines*, John Wiley & Sons, Ltd, 2014.
- [10] R. Hilzinger and W. Rodewald, *Magnetic materials: fundamentals, products, properties, applications*, Erlangen: Publicis Publishing, 2013, pp. 104-106.
- [11] H. Nakamura, K. Hirota, M. Shimao, T. Minowa and M. Honshima, "Magnetic properties of extremely small Nd-Fe-B sintered magnets," *IEEE Trans. Magn.*, vol. 41, DOI 10.1109/TMAG.2005.854874, no. 10, pp. 3844-3846, Oct. 2005.
- [12] T. Fukagawa and S. Hirosawa, "Coercivity generation of surface Nd<sub>2</sub>Fe<sub>14</sub>B grains and mechanism of fcc-phase formation at the Nd/Nd<sub>2</sub>Fe<sub>14</sub>B interface in Nd-sputtered Nd-Fe-B sintered magnets," *J. Appl. Phys.*, vol. 104, no. 1, pp. 1-6, Jul. 2008.
- [13] T. Woodcock *et al.*, "Understanding the microstructure and coercivity of high performance NdFeB-based magnets," *Scripta Materialia*, vol. 67, no. 6, pp. 536-541, Sept. 2012.
- [14] X. Fu, X. Han, Z. Du, H. Feng and Y. Li, "Microstructural investigation of Nd-rich phase in sintered Nd-Fe-B magnets through electron microscopy," *J. Rare Earths*, vol. 31, no. 8, pp. 765-771, Aug. 2013.
- [15] P.-A. Chen, C.-Y. Yang, S.-J. Chang, M.-H. Lee, N.-K. Tang, S.-C. Yen and Y.-C. Tseng, "Soft and hard natures of Nd<sub>2</sub>Fe<sub>14</sub>B permanent magnet explored by first-order-reversal-curves," *J. Magn. Magn. Mat.*, vol. 320, DOI 10.1016/j.jmmm.2014.06.027, pp. 45-53, 2014.
- [16] S. Bance *et al.*, "Influence of defect thickness on the angular dependence of coercivity in rare-earth permanent magnets," *Appl. Phys. Lett.*, vol. 104, no. 18, pp. 1-5, May 2014.
- [17] T. Schrefl, T. Shoji, M. Winklhofer, H. Oezelt, M. Yano and G. Zimanyi, "First order reversal curve studies of permanent magnets," *J. Appl. Phys.*, vol. 111, pp. 1-3, Apr. 2012.
- [18] H. Nishio, K. I. Machida and K. Ozaki, "More accurate hysteresis curve for large Nd-Fe-B sintered magnets employing a superconducting magnet-based vibrating sample magnetometer," *IEEE Trans. Magn.*, vol. 53, DOI 10.1109/TMAG.2016.2641399, no. 4, pp. 1-6, Apr. 2017.
- [19] R. G. Harrison, "Positive-Feedback Theory of Hysteretic Recoil Loops in Hard Ferromagnetic Materials," *IEEE Trans. Magn.*, vol. 47, DOI 10.1109/20.92151, no. 1, pp. 175-191, Jan. 2011.
- [20] E. Stenglein, D. Kuebrich, M. Albach and T. Duerbaum, "Guideline for hysteresis curve measurements with arbitrary excitation: pitfalls to avoid

and practices to follow," in *Intern. Exhib. and Conf. for Pow. Electron., Intel. Mot., Ren. En. and En. Manag.*, Nuremberg, 2018.

- [21] M. Takezawa, Y. Ichihara, Y. Morimoto and J. Yamasaki, "Surface Domain Configuration of Nd-Fe-B Sintered Magnets Influenced by Underneath Magnetization," *IEEE Trans. Magn.*, vol. 45, DOI: 10.1109/TMAG.2009.2021772, no. 10, pp. 4439-4442, Oct. 2009.
- [22] M. Katter, K. Ustuner and R. Blank, "Model for calculating J(H) curves of Ni coated Nd-Fe-B magnets," in *19th International Workshop on Rare Earth Permanent Magnets and their Applications*, China, 2006.
- [23] K. Hirota, H. Nakamura, T. Minowa and M. Honshima, "Coercivity enhancement by the grain boundary diffusion process to Nd-Fe-B sintered magnets," *IEEE Trans. Magn.*, vol. 42, no. 10, pp. 2909-2911, Oct. 2006.
- [24] R. G. Harrison, "Modelling high-order ferromagnetic hysteretic minor loops and spirals using positive feedback theory," *IEEE Trans. Magn.*, vol. 48, DOI 10.1109/TMAG.2011.2170846, no. 3, pp. 1115-1129, Mar. 2012.
- [25] Magnetic materials producer association, [Online]. Available: [www.allianceorg.com](http://www.allianceorg.com). [Accessed 28 Feb. 2019].
- [26] S. E. Zirka, Y. I. Moroz and R. G. Harrison, "Inverse hysteresis models for transient simulation," *IEEE Trans. Power Delivery*, vol. 29, DOI 10.1109/TPWRD.2013.2274530, no. 2, pp. 552-559, Apr. 2014.



**Dmitry Egorov** received the B.Sc. degree from the Moscow Power Engineering Institute, Moscow, Russia, in 2013, and the M.Sc. degree and D. Sc. (Tech.) degree in electrical engineering from the Lappeenranta-Lahti University of Technology (LUT), Lappeenranta, Finland, in 2015 and 2019, respectively. His research mainly concerns electrical machines and drives, in particular, the applications with the permanent magnets and development of new carbon-based materials for electrical machines.



**Ilya Petrov** received D.Sc. degree in 2015 from Lappeenranta University of Technology (LUT), Finland.

He is currently a fellow researcher in the Department of Electrical Engineering, LUT.



**Juha J. Pyrhönen** (M'06–SM'17) born in 1957 in Kuusankoski, Finland, received the Doctor of Science (D.Sc.) degree from Lappeenranta University of Technology (LUT), Finland in 1991. He became Professor of Electrical Machines and Drives in 1997 at LUT. He is engaged in research and development of electric motors and power-electronic-controlled drives. Prof. Pyrhönen has wide experience in the research and development of special electric drives for distributed

power production, traction drives and high-speed applications. Permanent magnet materials and applying them in machines have an important role in his research. Currently, he is also researching new carbon-based materials for electrical machines.



**Joosep Link** received the Master's degree in engineering physics from Tallinn University of Technology (TUT), Tallinn, Estonia, in 2016.

He is currently a Doctoral student at TUT and an early-stage researcher in the Department of Chemical Physics, National Institute of Chemical Physics and Biophysics, Tallinn, Estonia. His research interests include permanent magnets, multiferroics, and memristive materials.



**Raivo Stern** (M'16) received the M. Sc. Degree in condensed matter physics from Tartu University, and the Ph. D. (Solid State Physics) degree from Zurich University in 1987, and 1995, respectively.

He is currently a Research Professor in the Department of Chemical Physics of the National Institute of Chemical Physics and Biophysics (NICPB) in Tallinn, Estonia. His research interests are in the field of various modern materials, especially quantum magnets, strong permanent magnets, and unconventional superconductors.



**Peter Sergeant** (M'12–SM'19) received the MSc degree in electromechanical engineering in 2001, and the PhD degree in electromechanical engineering in 2006, both from Ghent University, Ghent, Belgium. In 2006, he became a post-doctoral researcher at Ghent University (post-doctoral fellow of the Research Foundation–Flanders). Since 2012, he is associate professor at Ghent University. He is also core lab manager in the cluster Motion Products of Flanders Make.

His research domain is electrical machines and drives for industrial and for sustainable energy applications. The focus is on accurate computation of losses in machines and drives, improving energy efficiency and increasing power density.



**Bulent Sarioglu** (M'94–SM'13) received the B.S. degree from Istanbul Technical University, Istanbul, Turkey, in 1990, the M.S. degree from the University of Missouri–Columbia, Columbia, MO, USA, in 1992, and the Ph.D. degree from the University of Wisconsin–Madison, Madison, WI, USA, in 1999, all in electrical engineering. Since 2011, he has been an Assistant Professor at the University of Wisconsin–Madison and the Associate Director of the Wisconsin Electric Machines and Power Electronics Consortium. From

2000 to 2011, he was with Honeywell International Inc.'s Aerospace Division, most recently as a Staff Systems Engineer in Torrance, CA, USA. His expertise includes electrical machines, drives, and power electronics and he is the inventor or coinventor of 16 U.S. patents as well as many international patents.